EUROPEAN ORGANISATION FOR NUCLEAR RESEARCH (CERN)

Submitted to: JHEP

CERN-EP-2022-143
18th July 2022

Measurement of the total and differential Higgs boson production cross-sections at $\sqrt{s} = 13$ TeV with the ATLAS detector by combining the $H \to ZZ^* \to 4\ell$ and $H \to \gamma\gamma$ decay channels

The ATLAS Collaboration

The total and differential Higgs boson production cross-sections are measured through a joint analysis of the $H \to ZZ^* \to 4\ell$ and $H \to \gamma\gamma$ decays. The results are based on a dataset of 139 fb^{-1} of proton–proton collisions recorded by the ATLAS detector at the Large Hadron Collider at a centre-of-mass energy of 13 TeV. The measured total Higgs boson production cross-section is $55.5^{+4.0}_{-3.8}$ pb, consistent with the Standard Model prediction of 55.6±2.8 pb. All results from the two decay channels are compatible with each other, and their combination agrees with the Standard Model predictions.

A joint interpretation of the measured Higgs boson fiducial transverse momentum distributions is performed and combined with measurement results from $H \to b\bar{b}/c\bar{c}$ to probe the Yukawa couplings to the bottom and charm quarks.

Contents

1 Introduction

Following the discovery of a Higgs boson (H) with a mass around 125 GeV ten years ago [1, 2], by the ATLAS and CMS collaborations at the Large Hadron Collider (LHC) at CERN, an intense programme to measure the properties of this particle and compare them with those of the Higgs boson predicted by the Standard Model (SM) of particle physics [3, 4] has been carried out.

In particular, total and differential fiducial Higgs boson production cross-sections have been measured, probing the kinematic features of the Higgs boson and of the particles produced in association with it. Both the ATLAS and CMS collaborations have measured total and differential fiducial Higgs boson production cross-sections at a proton–proton (pp) centre-of-mass energy $\sqrt{s}$ = 13 TeV in the $H \to ZZ^* \to 4\ell$ (where $\ell = e, \mu$) [5, 6], $H \to \gamma\gamma$ [7, 8], $H \to WW^* \to e\nu\mu\nu$ [9], and $H \to \tau\tau$ [10] decay channels. The collaborations have also performed combinations of some of the most sensitive results [11, 12]. The measurements are performed in fiducial volumes that significantly reduce the model dependence that would otherwise be introduced by relying on the acceptances predicted by the model under consideration to extrapolate the measured signal yields to the total phase space.

The most recent measurements of these cross-sections published by the ATLAS collaboration, exploiting 139 fb^{-1} [13, 14] of 13 TeV proton–proton collisions produced during the whole second data-taking phase of the LHC (Run 2, 2015–2018) and recorded by the ATLAS detector [15], have been performed using the $H \to ZZ^* \to 4\ell$ [5] and $H \to \gamma\gamma$ [7] final states.

The results of these two publications are combined in this article. The measurements are extrapolated to the full phase space and the measured cross-sections are compared with SM predictions. Additional systematic uncertainties introduced by the extrapolation to the full phase space are counterbalanced by a

significant reduction of the statistical uncertainty of the measurement, which is the main limitation to the precision of the measurements in the individual decay channels.

The measured observables include the total production cross-section and one and two-dimensional differential production cross-sections as a function of the Higgs boson transverse momentum[1] p_{T}^{H}, sensitive to perturbative QCD calculations, and of the Higgs boson rapidity $|y_H|$, sensitive to the parton distribution functions (PDF). Furthermore, differential cross-sections for jet multiplicity N_{jets} and the transverse momentum of the highest-p_{T} jet $p_{\mathrm{T}}^{\text{lead. jet}}$ are also measured. Both N_{jets} and $p_{\mathrm{T}}^{\text{lead. jet}}$ observables probe the theoretical modelling of high-p_{T} QCD radiation in Higgs boson production. These distributions are also sensitive to the different Higgs boson production processes. The measurements provide a stringent test of the SM predictions and any deviations from these predictions can indicate the presence of physics beyond the SM (BSM).

This article also presents a joint interpretation, in terms of the b- and c-quark Yukawa coupling strengths to the Higgs boson, of the fiducial differential cross-sections measured as a function of p_{T}^{H} in the two decay channels. Another interpretation, also including the constraints on the b and c Yukawa coupling strengths obtained from the measurements of Higgs boson production in association with a W or Z boson, with the Higgs boson decaying to b- or c-quark pairs [16, 17], is presented.

The results presented in this article update and supersede those of a previous publication [11] based on the same final states and a partial Run 2 dataset corresponding to an integrated luminosity of 36.1 fb^{-1}. With respect to the previous publication, both measurements included in this article use an improved jet reconstruction [18] and an improved unfolding procedure that is based on a detector response matrix included in the likelihood fit. Full descriptions of the measurements in the $H \to ZZ^* \to 4\ell$ and $H \to \gamma\gamma$ decay channels used in this article are given in Refs. [5, 7]. In both decay channels, the cross-sections in the full phase space are obtained from these unfolded yields by taking into account the luminosity, detector effects, fiducial acceptances, and branching fractions. The SM values of the Higgs boson branching fractions are assumed, and the acceptances are based on SM predictions. The value of the Higgs boson mass is assumed to be 125.09 GeV [19].

The paper is organised as follows. Section 2 describes the simulated Higgs boson event samples and inclusive theory cross-section calculations used to obtain the total and fiducial cross-section predictions. The signal acceptances for extrapolating the results to the total phase space are detailed in Section 3. The statistical procedure for the combination of the two channels is illustrated in Section 4, yielding the results summarised in Section 5. The differential cross-sections measured as a function of p_{T}^{H} are then used to constrain the Yukawa couplings of the Higgs boson to the bottom and charm quarks in Section 6.

2 Higgs boson simulation samples and theoretical predictions

The Monte Carlo (MC) event generators used for the calculation of the acceptance factors and detector effects, and for the SM predictions, are described in detail in Refs. [5, 7]. Their main features are summarised in this section.

[1] ATLAS uses a right-handed coordinate system with its origin at the nominal interaction point (IP) in the centre of the detector and the z-axis along the beam pipe. The x-axis points from the IP to the centre of the LHC ring, and the y-axis points upward. Cylindrical coordinates (r, ϕ) are used in the transverse plane, ϕ being the azimuthal angle around the z-axis. The pseudorapidity is defined in terms of the polar angle θ as $\eta = -\ln\tan(\theta/2)$.

Gluon–gluon fusion (ggF) events are simulated using POWHEG NNLOPS [20–30] with the PDF4LHC15 next-to-next-to-leading order (NNLO) set of parton distribution functions [31], while other production modes are simulated with POWHEG [20–22] with the PDF4LHC15 next-to-leading order (NLO) set except for $b\bar{b}H$ and tH, which are simulated using MADGRAPH5_AMC@NLO [32, 33] with the NNPDF3.0 NLO PDF set [34]. These samples are normalised to cross-sections obtained from the best available predictions as provided by the LHC Higgs Working Group [35] for a Higgs boson with a mass $m_H = 125.09$ GeV, which are 48.5 ± 2.4 pb, 3.78 ± 0.08 pb, 2.25 ± 0.06 pb, 0.49 ± 0.11 pb and 0.59 ± 0.05 pb for the ggF, VBF, VH, $b\bar{b}H$ and $t\bar{t}H + tH$ processes respectively. In the case of the ggF NNLOPS prediction, this corresponds to a rescaling to the fixed order N^{3}LO cross-section by a global K-factor of 1.1.

For all production mechanisms the PYTHIA 8.2 generator [36] is used to model the $H \to ZZ^* \to 4\ell$ and $H \to \gamma\gamma$ decays, as well as for the parton shower and the underlying event. The AZNLO set of tuned parameters [37] is used for ggF, VBF and VH production, while the A14 tune [38] is used for the other production modes. Alternative ggF, VBF, VH, $tH(t\bar{t}H)$ samples are produced by interfacing the nominal matrix element generator with HERWIG 7.1.3 (HERWIG 7.0.4) [39, 40], using the H7UE set of tuned parameters [40], in order to estimate uncertainties in the signal acceptance related to the modelling of the parton shower.

The measurements are also compared with an alternative prediction obtained by summing the expected cross-sections of non-ggF Higgs boson production processes described previously and an alternative SM ggF prediction obtained using MADGRAPH5_AMC@NLO (MG5 FxFx). This matrix-element generator provides NLO accuracy in QCD for zero, one, and two additional jets, using the FxFx merging scheme [32, 41], and includes the top and bottom quark mass effects [42–44]. The events are generated using the NNPDF30 NLO PDF set. The generator is interfaced to PYTHIA 8 for the modelling of the parton shower. The predicted cross-sections are scaled by a global N^{3}LO K-factor of 1.47.

Uncertainties in the predicted ggF, VBF, VH and $t\bar{t}H$ cross-sections induced by PDF uncertainties are estimated by varying the PDF4LHC set according to its eigenvectors [31], and summing in quadrature the variations in the predictions. The effect of PDF variations on the tH and $b\bar{b}H$ cross-sections has a negligible impact on the total uncertainty and is not included.

Uncertainties due to missing higher-order QCD effects for the ggF NNLOPS, VBF, VH and $t\bar{t}H$ predicted cross-sections are estimated using the same scheme as in Refs. [5, 7]: parameters accounting for cross-section and migration effects across various Higgs boson kinematic and associated jet observables are used and their variations are summed in quadrature. For other production modes, uncertainties related to missing higher-order QCD effects are estimated by varying the renormalisation and factorisation scales by factors of 0.5 and 2.0, and computing the difference between the envelope of the alternative predictions and the nominal one.

The Higgs boson branching ratios for $m_H = 125.09$ GeV are assumed to be those of the SM, $(0.0125 \pm 0.0003)\%$ for the four-lepton final state and $(0.227 \pm 0.007)\%$ for the diphoton final state [35].

3 Acceptance correction

The acceptance factors that extrapolate at particle-level from the respective $H \to ZZ^* \to 4\ell$ and $H \to \gamma\gamma$ fiducial phase spaces to the full phase space are estimated using the simulated event samples and cross-sections described in Section 2. The definitions of the fiducial phase spaces are summarised in Table 1 and Table 2, with more details provided in Refs. [5, 7] respectively. The evaluation of the acceptance factors

assumes SM Higgs boson production fractions and a Higgs boson mass of 125 GeV: the 90 MeV difference from the measured mass value of 125.09 GeV has a negligible impact on the Higgs boson kinematics.

Table 1: Summary of the particle-level fiducial definitions in the $H \to ZZ^* \to 4\ell$ analysis. A lepton *quadruplet* is formed by two same-flavour, opposite-charge (*SFOC*) lepton pairs. Dressed leptons are leptons whose four-momenta have been modified by adding the four-momenta of photons within a cone of size $\Delta R = 0.1$ around the lepton to account for final state radiation. The quadruplet satisfying the *lepton selection and pairing criteria* is labelled as the nominal quadruplet. If the nominal quadruplet fails the *event selection criteria*, no quadruplet is marked as the Higgs boson candidate. If the nominal quadruplet passes the selection and there is an additional lepton, the quadruplet with the largest ggF matrix element value is taken as the Higgs boson candidate. If no extra lepton is found, then the nominal quadruplet is taken as the Higgs boson candidate.

Lepton and jet definitions	
Leptons	Dressed leptons not originating from hadron or τ decays $p_{\mathrm{T}} > 5$ GeV, $\lvert\eta\rvert < 2.7$
Jets	$p_{\mathrm{T}} > 30$ GeV, $\lvert y\rvert < 4.4$
Lepton selection and pairing	
Lepton kinematics	p_{T} threshold for three leading leptons: $> 20, 15, 10$ GeV
Leading pair (m_{12})	SFOC lepton pair with smallest $\lvert m_Z - m_{\ell\ell}\rvert$
Subleading pair (m_{34})	Remaining SFOC lepton pair with smallest $\lvert m_Z - m_{\ell\ell}\rvert$ as nominal
Event selection	
Mass requirements	50 GeV$< m_{12} <$ 106 GeV and 12 GeV$< m_{34} <$ 115 GeV
Lepton separation	$\Delta R(\ell_i, \ell_j) > 0.1$
Lepton/Jet separation	$\Delta R(\ell_i, \text{jet}) > 0.1$
J/ψ veto	$m(\ell_i, \ell_j) > 5$ GeV for all SFOC lepton pairs
Mass window	105 GeV$< m_{4\ell} <$ 160 GeV
If extra lepton with $p_{\mathrm{T}} > 12$ GeV	Quadruplet with largest ggF matrix element value

Table 2: Summary of the particle-level fiducial definitions in the $H \to \gamma\gamma$ analysis. $E_{\mathrm{T}}^{\mathrm{iso}}(\Delta R, p_{\mathrm{T}}, \text{charged})$ is the scalar sum of the transverse momenta of charged stable particles with a transverse momentum above the specified threshold within a ΔR cone centred on the photon direction.

Photon and jet definitions	
Photons	Photons not originating from hadron decays $p_{\mathrm{T}} > 15$ GeV, $\lvert\eta\rvert < 1.37$ or $1.52 < \lvert\eta\rvert < 2.37$ $E_{\mathrm{T}}^{\mathrm{iso}}(\Delta R < 0.2, p_{\mathrm{T}} > 1$ GeV, charged$) < 0.05\, E_{\mathrm{T}}$
Jets	$p_{\mathrm{T}} > 30$ GeV, $\lvert y\rvert < 4.4$
Event selection	
Photon kinematics	p_{T} threshold for two leading photons: $p_{\mathrm{T}}^{\gamma_1} > 0.35 m_{\gamma\gamma}$, $p_{\mathrm{T}}^{\gamma_2} > 0.25 m_{\gamma\gamma}$
Mass window	105 GeV $< m_{\gamma\gamma} <$ 160 GeV

In the total phase space, the quantities p_{T}^H and $\lvert y_H\rvert$ are computed directly from the simulated Higgs boson momentum instead of its decay products, as in the fiducial analyses. The acceptance factors implicitly include the correction for this difference. Simulated particle-level jets are built from all stable particles

with $c\tau > 10$ mm, including neutrinos, photons, and leptons from hadron decays or produced in the shower. However, all decay products from the Higgs boson decay and the leptonic decays of associated vector bosons are removed from the inputs to the jet algorithm. Jets are reconstructed using the anti-k_t algorithm [45] with a radius parameter $R = 0.4$, and are required to have $p_{\mathrm{T}} > 30$ GeV.

Theory uncertainties related to the PDF, higher-order corrections, and the parton shower model are taken into account when evaluating acceptance factors. For each channel, the uncertainties on the acceptance factors are correlated with the impact of these theoretical sources on the detector response matrix used in the unfolding. Due to this procedure, compared with the results in Ref. [7], the $H \to \gamma\gamma$ results presented in this article have these additional theoretical uncertainties in the detector response matrix. Uncertainties due to the PDF and missing higher-order corrections are estimated as described in Section 2. Uncertainties due to the parton shower model are evaluated by comparing the acceptances estimated using MC samples with the default Pythia8 showering with the acceptances computed using MC samples relying on the Herwig7 showering model. To account for the uncertainties in the SM Higgs boson production cross-sections when calculating the total acceptance from the sum of the various production modes, the fractions of production modes are independently varied within their measured uncertainties taken from Ref. [46]. The total systematic uncertainties in the acceptance factors range between 0.5% and 7%, depending on the observable and bin, with the parton shower uncertainty being the dominant source.

The inclusive acceptance factors, relative to the full phase space, are about 50% for both the $H \to ZZ^* \to 4\ell$ and the $H \to \gamma\gamma$ channels. Figure 1 shows the acceptance factors and their systematic uncertainties as a function of p_{T}^H and N_{jets}. In the $H \to ZZ^* \to 4\ell$ channel, the acceptance factor drops in the highest p_{T}^H bin due to the lepton separation requirement, while the shape of the fiducial acceptance for the $H \to \gamma\gamma$ channel as a function of p_{T}^H is due to the p_{T} selection criteria on the photons.

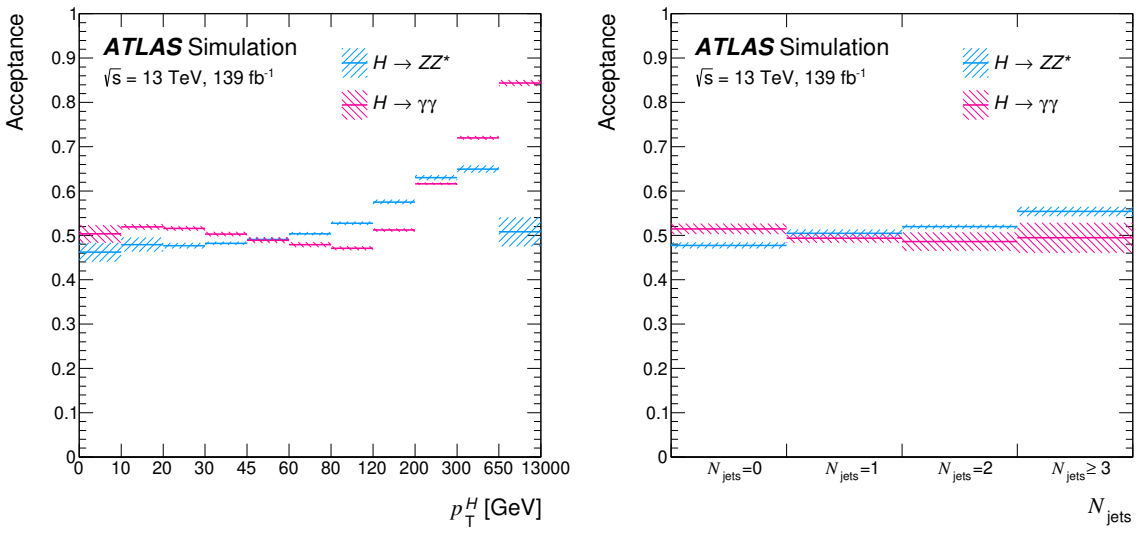

(a) (b)

Figure 1: Acceptance factors (solid lines), including systematic uncertainties (hatched bands), for the extrapolation from the fiducial to the total phase space for the $H \to ZZ^* \to 4\ell$ decay channel (blue) and the $H \to \gamma\gamma$ decay channel (magenta), as a function of variables characterising the Higgs boson kinematics: (a) Higgs boson transverse momentum p_{T}^H and (b) number of jets N_{jets} with $p_{\mathrm{T}} > 30$ GeV.

4 Statistical procedure

A likelihood combination of the two decay channels is performed, following the method described in Ref. [11]. For some observables, such as p_{T}^{H} and $p_{\mathrm{T}}^{\text{lead. jet}}$, the binning in the $H \to \gamma\gamma$ analysis is finer than that in the $H \to ZZ^* \to 4\ell$ analysis. Where needed, the sum of the consecutive $H \to \gamma\gamma$ sub-bins is combined with one $H \to ZZ^* \to 4\ell$ bin such that the measured bin boundaries match between the two results. A summary of the bin boundaries used in the combined results is presented in Table 3.

Table 3: Bin boundaries used in the combination of the cross-section of various differential observables. For the $p_{\mathrm{T}}^{\text{lead. jet}}$ distribution, the first bin contains all events with a leading jet with p_{T} less than 30 GeV, and corresponds exactly with the 0-jet bin in the N_{jets} differential distribution.

Variable	Bin Edges	N_{bins}
p_{T}^{H}	0, 10, 20, 30, 45, 60, 80, 120, 200, 300, 650, 13000 GeV	11
$\lvert y_H \rvert$	0, 0.15, 0.3, 0.45, 0.6, 0.75, 0.9, 1.2, 1.6, 2.0, 2.5	10
N_{jets}	0, 1, 2, ≥ 3	4
$p_{\mathrm{T}}^{\text{lead. jet}}$	0, 30, 60, 120, 350 GeV	4
p_{T}^{H} vs $\lvert y_H \rvert$	p_{T}^{H}: 0, 45, 120, 350 GeV; $\lvert y_H \rvert$: 0, 0.5, 1.0, 1.5, 2.5	12

Experimental and theoretical uncertainties that affect both channels are correlated via common nuisance parameters. The correlated experimental uncertainties include the uncertainties in the integrated luminosity, in the description of the pile-up in the simulation, in the jet reconstruction and calibration, in the common electron-photon energy scale, in the Higgs boson mass value, and in the contributions of the different Higgs boson production modes. Additionally, the common sources of theoretical uncertainty in the $H \to ZZ^* \to 4\ell$ and $H \to \gamma\gamma$ branching ratios (strong coupling constant, b and c quark masses, and partial decay widths to the main decay channels, such as two vector bosons, two gluons, or a $b\bar{b}$ pair) are also correlated. Finally, the theoretical uncertainties in the acceptance and response matrix due to missing higher-order QCD effects, PDF variations, variations of the modelling of the parton shower, and signal composition uncertainties are also correlated across the Higgs boson decay channels.

The asymptotic approximation [47] for the distribution of the profile likelihood ratio is assumed in the computation of uncertainties on all reported measurements. The validity of this approximation has been verified in previous analyses by performing pseudo-experiments.

5 Results

The total Higgs boson production cross-section at 13 TeV is measured to be $53.0^{+5.3}_{-5.1}$ pb ($^{+4.9}_{-4.8}$(stat.) $^{+2.0}_{-1.7}$(syst.)) using the $H \to ZZ^* \to 4\ell$ decay channel and $58.1^{+5.7}_{-5.4}$ pb (± 4.2(stat.) $^{+3.9}_{-3.5}$(syst.)) using the $H \to \gamma\gamma$ decay channel. The total cross-section obtained combining the two results is $55.5^{+4.0}_{-3.8}$ pb (± 3.2(stat.) $^{+2.4}_{-2.2}$(syst.)). All three results are in agreement with the SM prediction of 55.6 ± 2.8 pb. The measurements in the two decay channels are compatible with each other with a p-value of 49%, and the compatibility of the combined result with the SM prediction has a p-value of 98%. All compatibility checks are performed using a likelihood ratio approach, based on the test statistic variation under different hypotheses in the asymptotic approximation.

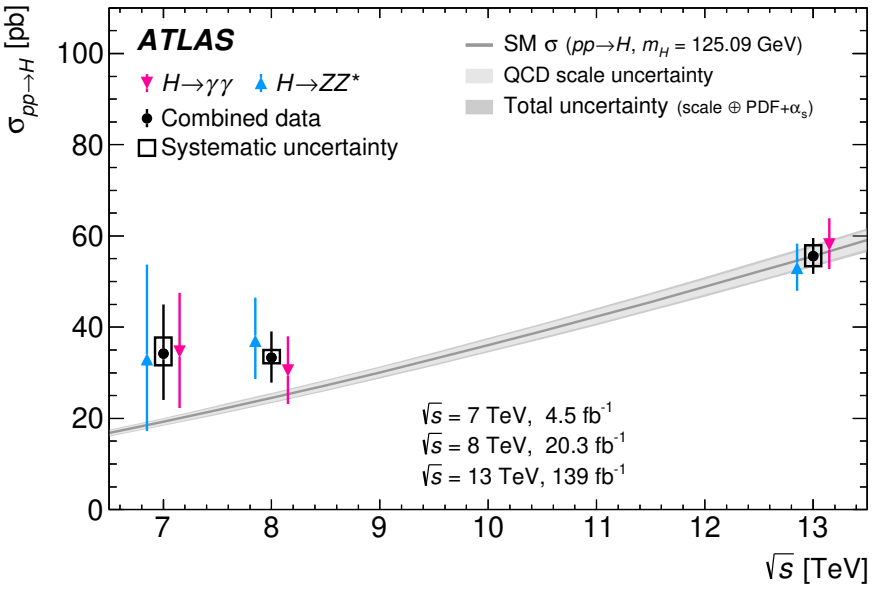

Figure 2: Total $pp \to H + X$ cross-sections measured at centre-of-mass energies of 7, 8 and 13 TeV, compared with Standard Model predictions taken from Ref. [35]. The measurements with the $H \to ZZ^* \to 4\ell$ channel (blue triangles), $H \to \gamma\gamma$ channel (magenta inverted triangles) and their combination (black dots) are shown. The individual channel results are offset along the x-axis for display purposes. The black boxes around the combined measurements represent the systematic uncertainty, while the error bars show the total uncertainty. The light grey band shows the uncertainty in the prediction due to missing higher-order corrections. The dark grey band indicates the total theoretical uncertainty, corresponding to the dominant higher-order-correction uncertainty summed in quadrature with the sum of the PDF and α_S uncertainties, and is partially correlated across values of the centre-of-mass energy.

The total cross-section measured using the two channels, their combination, and the SM prediction for a Higgs boson mass of 125.09 GeV are shown in Figure 2. The figure also includes the results of the measurements using data collected at a pp centre-of-mass energies of $\sqrt{s}$ = 8 TeV and 7 TeV, and the corresponding theoretical expectations. The event samples, selections and the cross-section measurement techniques used for the 8 TeV measurements are described in Refs. [48, 49]; similar techniques are used to measure the cross-sections at 7 TeV as described in Refs. [50, 51]. For both the 7 and 8 TeV results, the signal yields in the two decay channels are measured inclusively and corrected for acceptance and detector effects. The results at each centre-of-mass energy are then combined using a likelihood-based technique described in Ref. [52]. The total Higgs boson production cross-section at 7 TeV is measured to be 33^{+21}_{-16} pb using the $H \to ZZ^* \to 4\ell$ channel, 35^{+13}_{-16} pb using the $H \to \gamma\gamma$ decay channel, and 34^{+11}_{-10} pb (± 10(stat.) $^{+4}_{-2}$(syst.)) from their combination. This is to be compared with the SM expectation of 17.5 ± 1.6 pb. At 8 TeV, the total Higgs boson production cross-section is measured to be 37^{+9}_{-8} pb using the $H \to ZZ^* \to 4\ell$ channel, $30.5^{+7.5}_{-7.4}$ pb using the $H \to \gamma\gamma$ decay channel, and $33.3^{+5.8}_{-5.4}$ pb ($^{+5.5}_{-5.3}$(stat.) $^{+1.7}_{-1.3}$(syst.)) from their combination. This is to be compared with the SM expectation of 22.3 ± 2.0 pb. These results supersede the previously published ones, which used SM Higgs boson branching ratios calculated for a different value of the Higgs boson mass.

The differential cross-sections in bins of p_{T}^H, $|y_H|$, p_{T}^H vs $|y_H|$, N_{jets} and $p_{\mathrm{T}}^{\text{lead. jet}}$ for the individual channels and their combination are shown in Figures 3 and 4. The uncertainty band around the SM prediction includes PDF and α_S uncertainties as well as those due to missing higher-order corrections, obtained following the method described in Ref. [53]. When compared with the results from the individual

channels, the total uncertainty for the combined results is lower by 20%–40% and the impact of uncorrelated systematic uncertainties is reduced by approximately 40%. The observed correlation matrices among the cross-sections measured in different bins of the same observable are shown in Appendix A. The correlations are small (< 10%) for the Higgs-related observables (p_{T}^{H}, $|y_H|$), characterised by better experimental resolution, and larger (up to about 40%) for jet-related observables (N_{jets} and $p_{\mathrm{T}}^{\text{lead. jet}}$) with worse resolution and larger migrations.

All combined measurements are dominated by statistical uncertainties. Significant systematic uncertainties affecting the total and all differential cross-sections arise from the background modelling in the $H \to \gamma\gamma$ signal extraction [7] (typical error of 2–5%) and the integrated luminosity (1.7%). For the N_{jets} and $p_{\mathrm{T}}^{\text{lead. jet}}$ differential cross-section measurements, the uncertainties in the reconstruction of the jet energy scale and resolution are important as well, with impacts on the results typically in the range of 2–9%. The dominant theoretical source of uncertainty is the parton shower modelling for ggF signal and has an impact of 2–6%.

The p-values for the compatibility among the individual measurements are given in Table 4. The p-values for the compatibility of the measurements with various theoretical predictions are given in Table 5 for the differential cross-section results. For all observables, the measurements in the two channels are compatible with each other, with p-values ranging between 20% and 80%. The combined measurements are also in good agreement with the predictions, with p-values ranging between 20% and 98%. The prediction based on the NNLOPS simulation of gluon–gluon fusion events is lightly favoured over that based on the MG5 FxFx simulation.

Table 4: p-values in percent for the compatibility of the individual $H \to ZZ^* \to 4\ell$ and $H \to \gamma\gamma$ results for the combined total and differential cross-sections.

Observable	Total	p_{T}^{H}	$\lvert y_H \rvert$	p_{T}^{H} vs $\lvert y_H \rvert$	N_{jets}	$p_{\mathrm{T}}^{\text{lead. jet}}$
Compatibility p-value	49%	20%	23%	69%	80%	37%

Table 5: p-values in percent for the compatibility of the measured cross-sections with the SM predictions when the distributions for gluon–gluon fusion events obtained with either NNLOPS or MG5 FxFx, scaled to the fixed order N^{3}LO total gluon–gluon fusion cross-section, are used. The uncertainties in the theoretical predictions are included when calculating the p-values.

SM prediction	p_{T}^{H}	$\lvert y_H \rvert$	p_{T}^{H} vs $\lvert y_H \rvert$	N_{jets}	$p_{\mathrm{T}}^{\text{lead. jet}}$
NNLOPS	91%	98%	56%	95%	34%
MG5 FxFx	73%	98%	56%	86%	23%

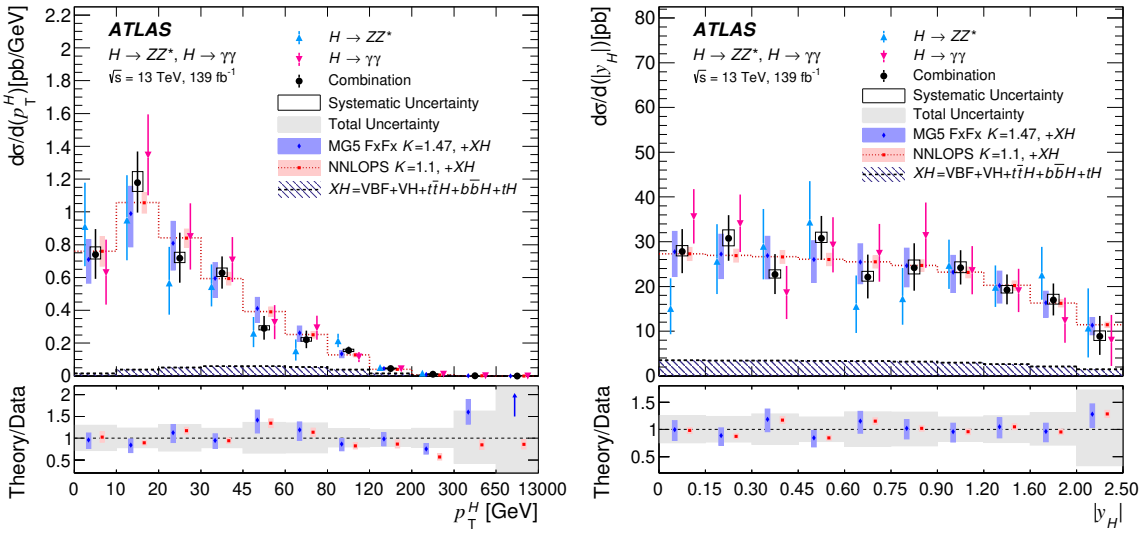

(a) (b)

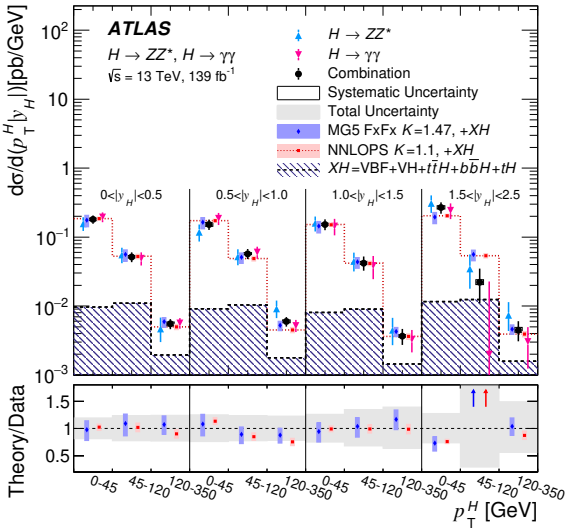

(c)

Figure 3: Differential $pp \to H + X$ cross-sections, in the full phase space, as a function of variables characterising the Higgs boson kinematics: (a) Higgs boson transverse momentum p_T^H, (b) Higgs boson rapidity $|y_H|$, and (c) p_T^H vs $|y_H|$, compared with Standard Model predictions. The $H \to ZZ^* \to 4\ell$ (blue triangles), $H \to \gamma\gamma$ (magenta inverted triangles), and combined (black squares) measurements are shown. The error bars on the data points show the total uncertainties, while the systematic uncertainties are indicated by the boxes. The measurements are compared with two predictions, obtained by summing the ggF predictions of NNLOPS or MG5 FxFx, normalised to the fixed order N^{3}LO total cross-section with the listed K-factors, and the MC predictions for the other production processes XH. The shaded bands indicate the relative impact of the PDF and scale systematic uncertainties in the prediction. These include the uncertainties related to the XH production modes. The dotted red histogram corresponds to the central value of the prediction that uses NNLOPS for the modelling of the ggF component. The bottom panels show the ratios between the predictions and the combined measurement. The grey area represents the total uncertainty of the measurement. For better visibility, all bins are shown as having the same size, independent of their numerical width.

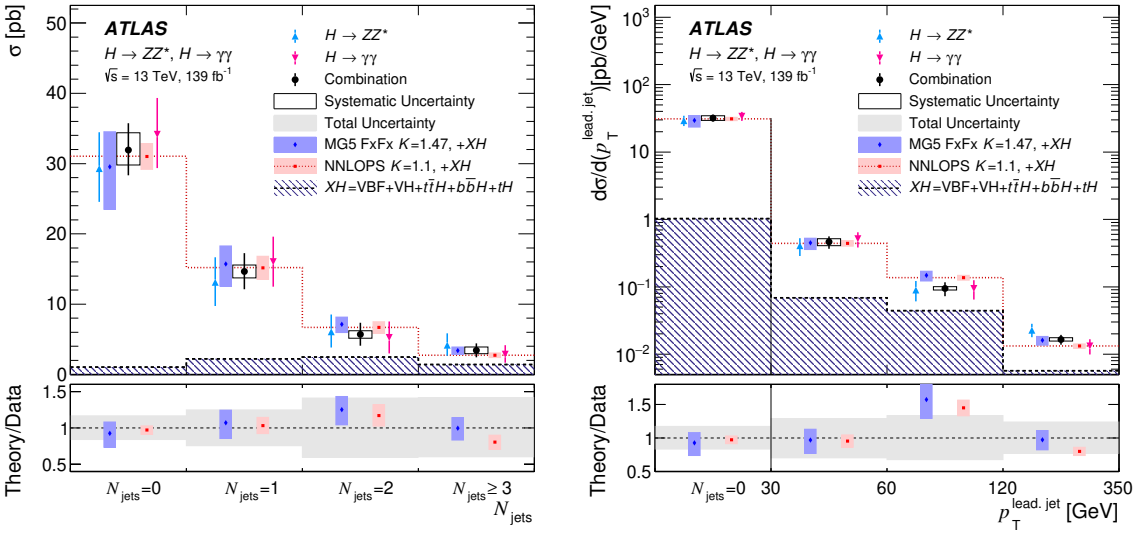

(a) (b)

Figure 4: Differential $pp \to H + X$ cross-sections, in the full phase space, as a function of variables related to the jets produced in association with the Higgs boson, (a) number of jets and (b) p_{T} of the leading jet, compared with Standard Model predictions. The figure uses the same layout as Figure 3.

6 Constraints on the b- and c-quark Yukawa couplings

The observations of the Higgs boson decays to $b\bar{b}$ [16, 54] provided stringent constraints on the possible modification of the b-quark Yukawa coupling with respect to its SM prediction, whereas current searches for Higgs boson decays to charm final states [17, 55] still allow for a relatively large modification of the c-quark coupling. These measurements have been interpreted in terms of the Yukawa coupling modifiers for b- and c-quarks, κ_b and κ_c, defined as multipliers of the SM values of these couplings [35]. The measured value of κ_b agrees with the SM prediction of one with a precision of about 10% [56] to 20% [57], whereas the constraints on κ_c are significantly looser: $|\kappa_c| < 5.7$ [56] or $1.1 < |\kappa_c| < 5.5$ [58] at the 95% confidence level (CL).

The Higgs boson p_{T} distribution is sensitive to modifications of the Yukawa couplings of the Higgs boson to the b- and c-quarks [59]. This sensitivity is driven by the contributions of b- and c-quarks to the loop-induced ggF production and by the quark-initiated production of the Higgs boson. The former production mode includes an interference term between b- and c-quark loop-mediated amplitudes which is proportional to the product of the two couplings and is therefore sensitive to their relative sign. Modifications of the coupling strength to b- and c-quarks result in changes to both the overall cross-section and the shape of the p_{T}^H distribution. In addition, the branching ratio for the $H \to \gamma\gamma$ decay would be affected by corresponding changes to its partial decay width, and both the $H \to ZZ^* \to 4\ell$ and $H \to \gamma\gamma$ branching ratios would also be affected by the changes to the total Higgs boson decay width.

This section presents constraints on κ_b and κ_c, inferred from the measured p_{T}^H distributions. A combined interpretation is then performed in terms of κ_b and κ_c by including also the constraints from the measurement of Higgs bosons, produced in association with a vector boson, decaying to $b\bar{b}$ [16], and from the search for Higgs bosons produced in a similar way and decaying to $c\bar{c}$ [17]. All tree-level couplings of the Higgs boson to particles other than the b- or c-quarks are set to their SM values and loop-induced Higgs boson couplings are resolved to their SM expectation, with κ_b and κ_c as free parameters.

6.1 Constraints from the Higgs boson transverse momentum distributions

The constraints on κ_b and κ_c from the observed p_{T}^H distributions in the $H \to ZZ^* \to 4\ell$ and $H \to \gamma\gamma$ final states are derived in two scenarios: one in which only modification to the shape of the measured p_{T}^H distributions is considered ("*shape-only*"), and one in which the impact on the overall expected normalisation, through modifications of the total cross-sections, branching ratios and Higgs boson decay width, is also considered ("*shape+normalisation*").

The theoretical predictions used for these interpretations are detailed in Ref. [7]. The predictions for κ_b and κ_c modifications of the ggF production are computed with SCETlib [60, 61]. For the $H \to \gamma\gamma$ decay channel, these calculations are performed for its fiducial phase space, while for the $H \to ZZ^* \to 4\ell$ decay channel, the inclusive predictions are extrapolated to the fiducial phase space using the acceptances obtained from the NNLOPS ggF prediction. It has been verified that the dependence of the acceptance factors in each p_{T}^H bin on the b and c Yukawa coupling modifiers is negligible. The predictions for quark-initiated $b\bar{b} \to H$ and $c\bar{c} \to H$ production modes are computed with MadGraph5_aMC@NLO 2.7.3. The simulation of the Higgs boson decay, the parton shower, hadronisation and underlying event, is performed with Pythia 8 using a dedicated PDF set [62] and the A14 tune. The inclusive $b\bar{b} \to H$ and $c\bar{c} \to H$ cross-sections are then normalised to the state-of-the-art NNLO computations available in Refs. [62, 63].

All the other Higgs boson production modes remain unchanged with κ_b and κ_c variations, and they are estimated as detailed in Section 2.

Theoretical uncertainties related to the QCD modelling and PDF uncertainties on the differential cross-sections are considered using the procedure detailed in Ref. [7]. For the theoretical calculation of the ggF process, uncertainties related to numerical integration, fixed-order scale, hard resummation phase, resummation scheme, matching scale and non-perturbative scheme are implemented [60]. For the b- and c-quark initiated processes, the uncertainty related to missing higher order QCD effects are estimated by varying the renormalisation, factorisation and merging scales; the uncertainties related to the PDF set are estimated by varying the mass and scale associated with the b-quark for the $b\bar{b} \to H$ process and by using the MC replicas of the nominal PDF set for the $c\bar{c} \to H$ process; the uncertainties due to the choice of the FxFx merging scale are estimated by using alternative values of this scale. Theoretical uncertainties in the other production modes that do not depend on κ_b or κ_c, from higher-order QCD effects, PDF and α_s, and the parton shower model, are estimated as described in Section 2.

The statistical interpretation is performed by first parameterising the fiducial cross-sections as a function of κ_b and κ_c for each decay channel. The two likelihood models are then jointly interpreted using the same procedure as detailed in Section 4.

Table 6: Observed and expected 95% confidence intervals for the Yukawa coupling modifiers when modifications to only the p_{T}^{H} shape are considered (*shape-only*), for the individual decay channels and their combination. The results for one coupling modifier are obtained while fixing the other one to the SM expectation ($\kappa = 1$).

Channel	Parameter	Observed 95% confidence interval	Expected 95% confidence interval
$H \to ZZ^* \to 4\ell$	κ_b	$[-1.8,\ 6.4]$	$[-3.3,\ 9.3]$
	κ_c	$[-7.7,\ 18.3]$	$[-12.3,\ 19.2]$
$H \to \gamma\gamma$	κ_b	$[-3.5,\ 10.2]$	$[-2.5,\ 8.0]$
	κ_c	$[-12.6,\ 18.3]$	$[-10.1,\ 17.3]$
Combined	κ_b	$[-2.0,\ 7.4]$	$[-2.0,\ 7.4]$
	κ_c	$[-8.6,\ 17.3]$	$[-8.5,\ 15.9]$

The best-fit values, expected and observed 95% confidence intervals for κ_b and κ_c are shown in Tables 6 and 7 for the *shape-only* and *shape+normalisation* scenarios, respectively. The limits on a given κ parameter are determined with the other one fixed to SM prediction ($\kappa = 1$). If κ_b is unconstrained in the fit, the 95% confidence intervals for κ_c are about 10% (twice) larger than if κ_b is fixed to the SM value of one, in the *shape-only* (*shape+normalisation*) approach.

In the *shape-only* approach, the combined expected limits on κ_b are better than the results from the individual channels, while the combined observed limits are less stringent than the individual $H \to ZZ^* \to 4\ell$ result. This is due to quadratic dependency of the cross-section and the differential distribution on the κ parameters leading to a double minimum in the profile likelihood ratio, and due to the combined best-fit value for the κ_b parameter being further from the SM expectation when probing only the $H \to \gamma\gamma$ decay channel. For κ_c, the observed combined best-fit value is similar to the best-fit value in the $H \to ZZ^* \to 4\ell$ channel. However, due to the correlation between the κ_b and κ_c parameters, different best-fit κ_b observations between the channels, as well as the data fluctuations in some of the p_{T}^{H} bins, the 68% CL observed

combined limits on κ_c are worse than the results from the $H \to ZZ^* \to 4\ell$ channel. The corresponding 95% CL limits are similar to those from the $H \to ZZ^* \to 4\ell$ channel.

In the *shape+normalisation* scenario the constraints on the coupling modifiers are tighter, since a large fraction of the allowed ranges for κ_b and κ_c from the *shape-only* approach lead to values of the total width and thus of the $H \to ZZ^* \to 4\ell$ and $H \to \gamma\gamma$ branching ratios and overall normalisation that are inconsistent with the data.

Two-dimensional confidence regions on κ_b and κ_c are also derived for both scenarios, as shown in Figure 5.

Table 7: Observed and expected 95% confidence intervals for the Yukawa coupling modifiers when modifications to both the p_{T}^H shape and normalisation are considered (*shape+normalisation*), for the individual decay channels and their combination. The results for one coupling modifier are obtained while fixing the other one to the SM expectation ($\kappa = 1$).

Channel	Parameter	Observed 95% confidence interval	Expected 95% confidence interval
$H \to ZZ^* \to 4\ell$	κ_b	$[-1.14, -0.88] \cup [0.80, 1.17]$	$[-1.23, -0.87] \cup [0.82, 1.20]$
	κ_c	$[-2.94,\ 2.99]$	$[-3.33, 3.14]$
$H \to \gamma\gamma$	κ_b	$[-1.12, -0.78] \cup [0.78, 1.07]$	$[-1.18, -0.87] \cup [0.83, 1.19]$
	κ_c	$[-2.46,\ 2.32]$	$[-3.03,\ 3.09]$
Combined	κ_b	$[-1.09, -0.86] \cup [0.81, 1.09]$	$[-1.14, -0.92] \cup [0.86, 1.15]$
	κ_c	$[-2.27,\ 2.27]$	$[-2.77,\ 2.75]$

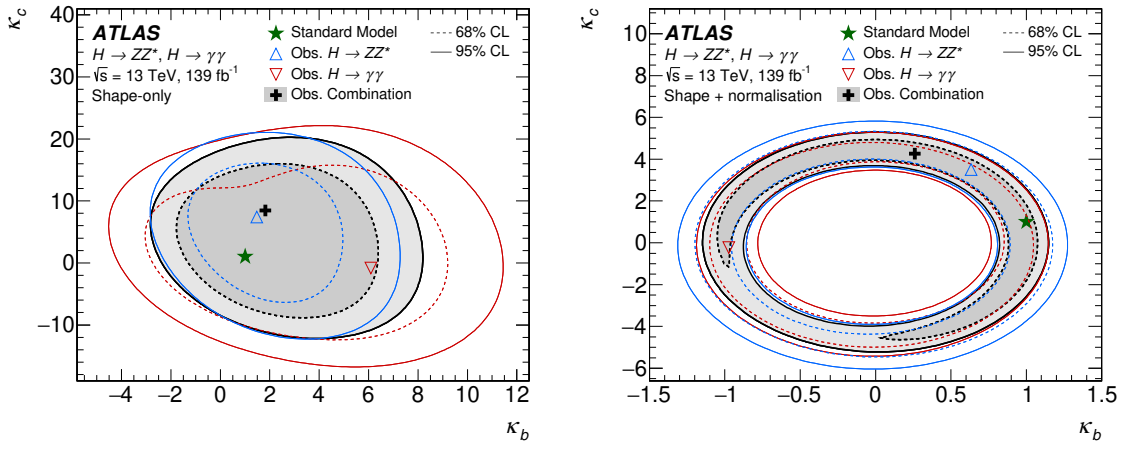

(a) (b)

Figure 5: Observed limits at 95% CL on the Yukawa coupling modifiers κ_b and κ_c when (a) only the shape of the p_{T}^H differential cross-section (*shape-only*) or (b) also its normalisation (*shape+normalisation*) is used to constrain the parameters for the combined and individual decay channels results. The SM predictions ($*$) and the observed best-fit values (+) are indicated on the plots.

6.2 Combination with the constraints from $VH(b\bar{b})$ and $VH(c\bar{c})$ production

The measurement of Higgs boson decays to $b\bar{b}$ and the search for Higgs boson decays to $c\bar{c}$ in Higgsstrahlung events (VH) constrain the b- and c-quark coupling modifiers through the quadratic dependence on κ_b^2 and κ_c^2 of the partial widths of the Higgs boson to these two final states. This section describes the methodology and the results of a simultaneous fit to the Higgs boson transverse momentum distributions of the $H \to ZZ^* \to 4\ell$ and $H \to \gamma\gamma$ fiducial cross section measurements and to the multivariate discriminant used to measure the $VH(q\bar{q})$ ($q = b, c$) signal strength [16, 17].

Two scenarios are considered for this combination. The first scenario is the "*shape+normalisation*" scenario as described previously. In the second scenario, the Higgs boson is also allowed to decay to BSM particles and the associated partial width is included in the total width. The partial width for BSM decays is parameterised as $\Gamma_{\text{BSM}} = \Gamma \times B_{\text{BSM}} = \Gamma_{\text{SM}} \frac{B_{\text{BSM}}}{1-B_{\text{BSM}}}$, where Γ is the Higgs boson total width, and B_{BSM} is its branching ratio to BSM particles. The second scenario reduces the assumptions of the model, at the cost of reduced sensitivity.

In the combination, most common experimental systematic uncertainties and signal theory uncertainties are modelled as correlated between the four channels ($H \to ZZ^* \to 4\ell$, $H \to \gamma\gamma$, $VH(b\bar{b})$, $VH(c\bar{c})$). Jet energy calibration and flavour tagging efficiency uncertainties are not modelled as correlated between the channels due to the use of different jet clustering algorithms.

The observed 68% and 95% CL contours in the 2D κ_b vs κ_c plane are shown in Figure 6(a) for the *shape+normalisation* scenario where B_{BSM} is fixed to zero and in Figure 6(b) for the case where B_{BSM} is a free parameter. The fit prefers a positive value of κ_b, but negative values are not excluded at 68% CL, leading to two disconnected allowed regions, corresponding to positive or negative values of κ_b. One-dimensional confidence intervals for κ_c with κ_b unconstrained in the fit are summarised in Table 8. Excluding the $VH(c\bar{c}$ channel would worsen the one-dimensional constraints on κ_c by about 10% for the $B_{\text{BSM}} = 0$ scenario, and by a factor two for the alternative scenario where B_{BSM} is not fixed to zero.

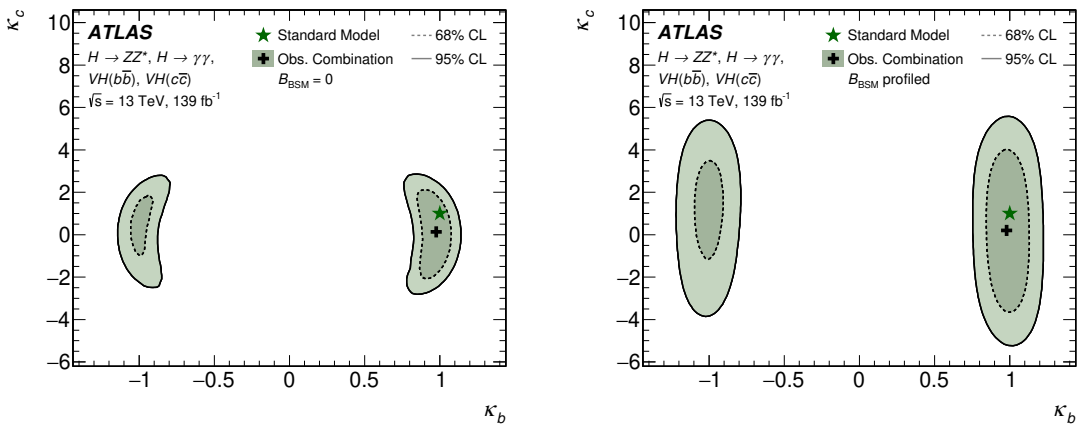

(a) (b)

Figure 6: Observed 2D negative log likelihood contours for the κ_b and κ_c parameters from a simultaneous fit to the Higgs p_{T} fiducial cross-sections in $H \to \gamma\gamma$ and $H \to ZZ^* \to 4\ell$ and to multivariate discriminants used to identify VH events with Higgs bosons decaying to $b\bar{b}$ or $c\bar{c}$, for (a) $B_{\text{BSM}} = 0$ or (b) leaving B_{BSM} unconstrained.

Table 8: One-dimensional confidence intervals in κ_c, while profiling κ_b, at 68% and 95% CL, obtained from a simultaneous fit to fiducial cross-sections in $H \to ZZ^* \to 4\ell$ and $H \to \gamma\gamma$ in bins of the Higgs boson p_{T} and to VH data with Higgs bosons decaying to $b\bar{b}$ or $c\bar{c}$.

Scenario	Observed 68% confidence interval	Observed 95% confidence interval
$B_{\mathrm{BSM}} = 0$	$[-1.61, 1.70]$	$[-2.47, 2.53]$
No assumption on B_{BSM}	$[-2.63, 3.01]$	$[-4.46, 4.81]$

7 Conclusions

A combined measurement of the total and differential Higgs production cross-sections in the $H \to \gamma\gamma$ and $H \to ZZ^* \to 4\ell$ decay channels was performed using 139 fb^{-1} of 13 TeV proton–proton collision recorded by the ATLAS detector during the LHC Run 2. Good agreement is observed when comparing the results from the two channels, after extrapolation to a common phase space. The total Higgs boson production cross-section is measured with an unprecedented precision of 7%, comparable to that of the best avaliable Standard Model prediction which is 5%. The result, $55.5^{+4.0}_{-3.8}$ pb, agrees with the SM predicted value of 55.6 ± 2.8 pb.

Differential cross-sections are measured as a function of the Higgs boson transverse momentum and rapidity, the number of jets produced together with the Higgs boson and the transverse momentum of the leading jet. The larger data set and the combination of the two decay channels result in measurement uncertainties that are significantly smaller than in previous results. Notably, the differential cross-section as a function of the Higgs boson transverse momentum is measured with 20–30% precision up to 300 GeV and about 60% precision in the 300–650 GeV range. The combined differential distributions agree with the Standard Model predictions.

The measured fiducial differential cross-sections as a function of p_{T}^H are used to derive limits on the bottom and charm-quark Yukawa couplings modifiers, κ_b and κ_c, assuming SM values of the other tree-level Higgs boson couplings. Fixing the value of κ_b to one, the 95% confidence interval for κ_c is $[-8.6, 17.3]$ using only the observed shape of the p_{T}^H distribution, and $[-2.27, 2.27]$ when considering also the impact of these couplings on the normalisation of the measured p_{T}^H fiducial cross-sections.

A combined fit with the ATLAS measurement of Higgs bosons produced in association with a W or Z boson and decaying to b- or c-quark pairs allows constraints to be set on the charm quark coupling modifier without any assumption on the bottom quark coupling. The 95% CL allowed range for κ_c when the Higgs boson is assumed to decay only to SM particles is $[-2.47, 2.53]$ while in a more generic scenario in which BSM Higgs boson decays are allowed, the constraint is loosened to $[-4.46, 4.81]$. These represent the most stringent constraints on κ_c to date in these scenarios.

Appendix

A Correlation matrices between the measured cross-sections

Figure 7 and Figure 8 show the correlation matrices among the differential cross-sections measured in different bins of the same one-dimensional measurement.

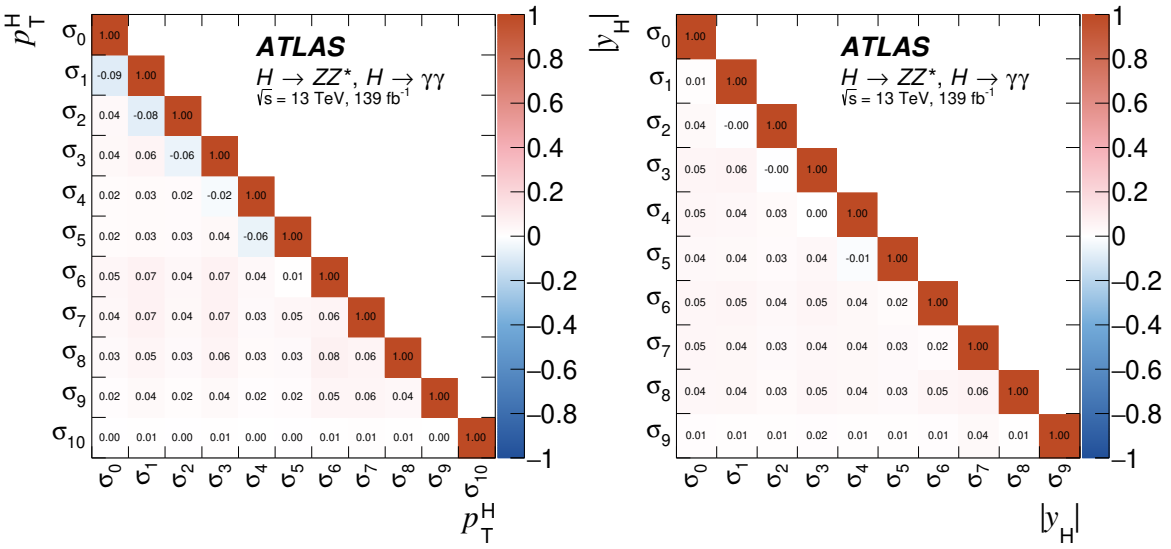

(a) (b)

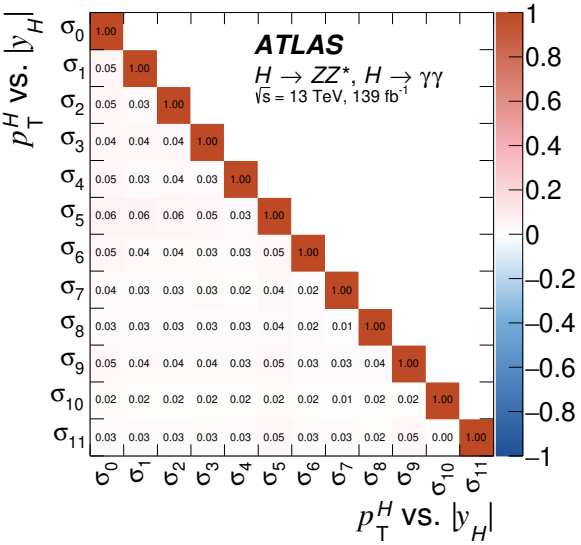

(c)

Figure 7: Correlation matrices between the differential $pp \to H + X$ cross-sections measured in different bins of the same observable: (a) Higgs boson transverse momentum, (b) Higgs boson rapidity and (c) Higgs boson transverse momentum vs Higgs boson rapidity. The labels are defined as per the bin boundaries outlined in Table 3, with a higher label index corresponding to a higher bin for the given variable. For the correlation matrix for the Higgs boson transverse momentum vs Higgs boson rapidity, lower rapidity bins are labelled first with ascending bins in p_T^H.

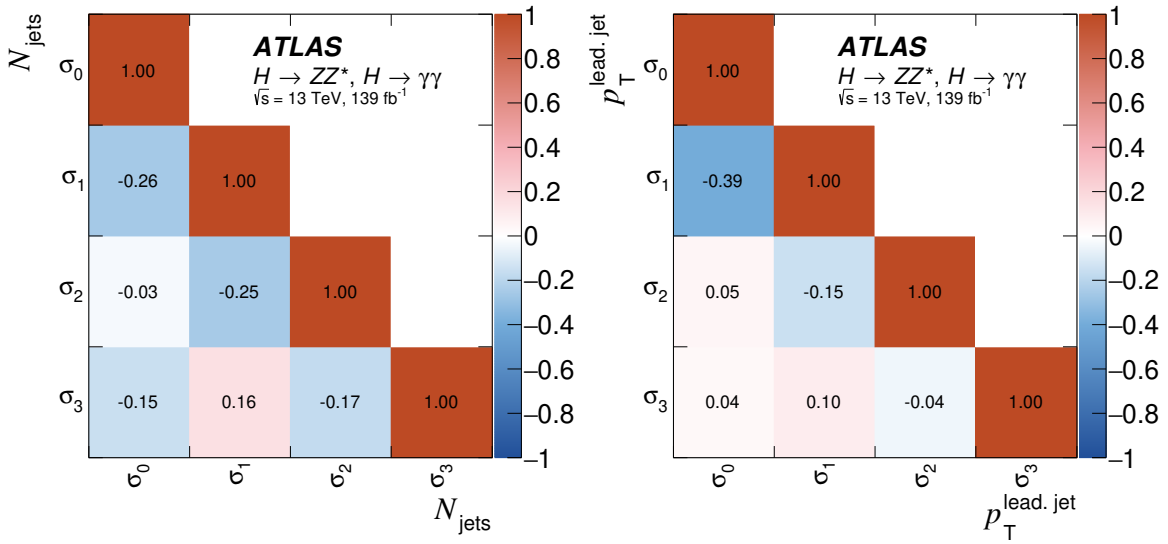

(a) (b)

Figure 8: Correlation matrices between the differential $pp \to H + X$ cross-sections measured in different bins of the same observable: (a) number of jets and (b) p_{T} of the leading jet. The labels are defined as per the bin boundaries outlined in Table 3, with a higher label index corresponding to a higher bin for the given variable.

References

[1] ATLAS Collaboration, *Observation of a new particle in the search for the Standard Model Higgs boson with the ATLAS detector at the LHC*, Phys. Lett. B **716** (2012) 1, arXiv: 1207.7214 [hep-ex].

[2] CMS Collaboration, *Observation of a new boson at a mass of 125 GeV with the CMS experiment at the LHC*, Phys. Lett. B **716** (2012) 30, arXiv: 1207.7235 [hep-ex].

[3] F. Englert and R. Brout, *Broken Symmetry and the Mass of Gauge Vector Mesons*, Phys. Rev. Lett. **13** (1964) 321, ed. by J. C. Taylor.

[4] P. W. Higgs, *Broken symmetries, massless particles and gauge fields*, Phys. Lett. **12** (1964) 132.

[5] ATLAS Collaboration, *Measurements of the Higgs boson inclusive and differential fiducial cross sections in the 4ℓ decay channel at $\sqrt{s}$ = 13 TeV*, Eur. Phys. J. C **80** (2020) 942, arXiv: 2004.03969 [hep-ex].

[6] CMS Collaboration, *Measurements of production cross sections of the Higgs boson in the four-lepton final state in proton–proton collisions at $\sqrt{s}$ = 13 TeV*, Eur. Phys. J. C **81** (2021) 488, arXiv: 2103.04956 [hep-ex].

[7] ATLAS Collaboration, *Measurements of the Higgs boson inclusive and differential fiducial cross-sections in the diphoton decay channel with 139 fb^{-1} of pp collisions at $\sqrt{s}$ = 13 TeV with the ATLAS detector*, CERN-EP-2021-227 (2022), arXiv: 2202.00487 [hep-ex].

[8] CMS Collaboration, *Measurement of inclusive and differential Higgs boson production cross sections in the diphoton decay channel in proton–proton collisions at* $\sqrt{s} = 13$ *TeV*, JHEP **01** (2019) 183, arXiv: 1807.03825 [hep-ex].

[9] CMS Collaboration, *Measurement of the inclusive and differential Higgs boson production cross sections in the leptonic WW decay mode at* $\sqrt{s} = 13$ *TeV*, JHEP **03** (2021) 003, arXiv: 2007.01984 [hep-ex].

[10] CMS Collaboration, *Measurement of the inclusive and differential Higgs boson production cross sections in the decay mode to a pair of* τ *leptons in* pp *collisions at* $\sqrt{s} = 13$ *TeV*, Phys. Rev. Lett. **128** (2021) 081805, arXiv: 2107.11486 [hep-ex].

[11] ATLAS Collaboration, *Combined measurement of differential and total cross sections in the* $H \to \gamma\gamma$ *and the* $H \to ZZ^* \to 4\ell$ *decay channels at* $\sqrt{s} = 13$ *TeV with the ATLAS detector*, Phys. Lett. B **786** (2018) 114, arXiv: 1805.10197 [hep-ex].

[12] CMS Collaboration, *Measurement and interpretation of differential cross sections for Higgs boson production at* $\sqrt{s} = 13$ *TeV*, Phys. Lett. B **792** (2019) 369, arXiv: 1812.06504 [hep-ex].

[13] ATLAS Collaboration, *Luminosity determination in* pp *collisions at* $\sqrt{s} = 13$ *TeV using the ATLAS detector at the LHC*, ATLAS-CONF-2019-021, 2019, URL: https://cds.cern.ch/record/2677054.

[14] G. Avoni et al., *The new LUCID-2 detector for luminosity measurement and monitoring in ATLAS*, JINST **13** (2018) P07017.

[15] ATLAS Collaboration, *The ATLAS Experiment at the CERN Large Hadron Collider*, JINST **3** (2008) S08003.

[16] ATLAS Collaboration, *Measurements of* WH *and* ZH *production in the* $H \to b\bar{b}$ *decay channel in* pp *collisions at* 13 *TeV with the ATLAS detector*, Eur. Phys. J. C **81** (2021) 178, arXiv: 2007.02873 [hep-ex].

[17] ATLAS Collaboration, *Direct constraint on the Higgs-charm coupling from a search for Higgs boson decays into charm quarks with the ATLAS detector*, CERN-EP-2021-251 (2022), arXiv: 2201.11428 [hep-ex].

[18] ATLAS Collaboration, *Jet reconstruction and performance using particle flow with the ATLAS Detector*, Eur. Phys. J. C **77** (2017) 466, arXiv: 1703.10485 [hep-ex].

[19] ATLAS and CMS Collaborations, *Combined Measurement of the Higgs Boson Mass in* pp *Collisions at* $\sqrt{s} = 7$ *and* 8 *TeV with the ATLAS and CMS Experiments*, Phys. Rev. Lett. **114** (2015) 191803, arXiv: 1503.07589 [hep-ex].

[20] P. Nason, *A New method for combining NLO QCD with shower Monte Carlo algorithms*, JHEP **11** (2004) 040, arXiv: hep-ph/0409146.

[21] S. Frixione, P. Nason and C. Oleari, *Matching NLO QCD computations with parton shower simulations: the POWHEG method*, JHEP **11** (2007) 070, arXiv: 0709.2092 [hep-ph].

[22] S. Alioli, P. Nason, C. Oleari and E. Re, *A general framework for implementing NLO calculations in shower Monte Carlo programs: the POWHEG BOX*, JHEP **06** (2010) 043, arXiv: 1002.2581 [hep-ph].

[23] K. Hamilton, P. Nason, E. Re and G. Zanderighi, *NNLOPS simulation of Higgs boson production*, JHEP **10** (2013) 222, arXiv: 1309.0017 [hep-ph].

[24] K. Hamilton, P. Nason and G. Zanderighi, *Finite quark-mass effects in the NNLOPS POWHEG+MiNLO Higgs generator*, JHEP **05** (2015) 140, arXiv: 1501.04637 [hep-ph].

[25] K. Hamilton, P. Nason and G. Zanderighi, *MINLO: multi-scale improved NLO*, JHEP **10** (2012) 155, arXiv: 1206.3572 [hep-ph].

[26] J. M. Campbell et al., *NLO Higgs boson production plus one and two jets using the POWHEG BOX, MadGraph4 and MCFM*, JHEP **07** (2012) 092, arXiv: 1202.5475 [hep-ph].

[27] K. Hamilton, P. Nason, C. Oleari and G. Zanderighi, *Merging H/W/Z + 0 and 1 jet at NLO with no merging scale: a path to parton shower + NNLO matching*, JHEP **05** (2013) 082, arXiv: 1212.4504 [hep-ph].

[28] S. Catani and M. Grazzini, *Next-to-Next-to-Leading-Order Subtraction Formalism in Hadron Collisions and its Application to Higgs-boson Production at the Large Hadron Collider*, Phys. Rev. Lett. **98** (2007) 222002, arXiv: hep-ph/0703012 [hep-ph].

[29] G. Bozzi, S. Catani, D. de Florian and M. Grazzini, *Transverse-momentum resummation and the spectrum of the Higgs boson at the LHC*, Nucl. Phys. B **737** (2006) 73, arXiv: hep-ph/0508068 [hep-ph].

[30] D. de Florian, G. Ferrera, M. Grazzini and D. Tommasini, *Transverse-momentum resummation: Higgs boson production at the Tevatron and the LHC*, JHEP **11** (2011) 064, arXiv: 1109.2109 [hep-ph].

[31] J. Butterworth et al., *PDF4LHC recommendations for LHC Run II*, J. Phys. G **43** (2016) 023001, arXiv: 1510.03865 [hep-ph].

[32] J. Alwall et al., *The automated computation of tree-level and next-to-leading order differential cross sections, and their matching to parton shower simulations*, JHEP **07** (2014) 079, arXiv: 1405.0301 [hep-ph].

[33] M. Wiesemann et al., *Higgs production in association with bottom quarks*, JHEP **02** (2015) 132, arXiv: 1409.5301 [hep-ph].

[34] R. D. Ball et al., *Parton distributions for the LHC run II*, JHEP **04** (2015) 040, arXiv: 1410.8849 [hep-ph].

[35] D. de Florian et al., *Handbook of LHC Higgs Cross Sections: 4. Deciphering the Nature of the Higgs Sector*, (2016), arXiv: 1610.07922 [hep-ph].

[36] T. Sjöstrand et al., *An introduction to PYTHIA 8.2*, Comput. Phys. Commun. **191** (2015) 159, arXiv: 1410.3012 [hep-ph].

[37] ATLAS Collaboration, *Measurement of the Z/γ^* boson transverse momentum distribution in pp collisions at $\sqrt{s} = 7$ TeV with the ATLAS detector*, JHEP **09** (2014) 145, arXiv: 1406.3660 [hep-ex].

[38] ATLAS Collaboration, *ATLAS Pythia 8 tunes to 7 TeV data*, ATL-PHYS-PUB-2014-021, 2014, URL: https://cds.cern.ch/record/1966419.

[39] M. Bähr et al., *Herwig++ physics and manual*, Eur. Phys. J. C **58** (2008) 639, arXiv: 0803.0883 [hep-ph].

[40] J. Bellm et al., *Herwig 7.0/Herwig++ 3.0 release note*, Eur. Phys. J. C **76** (2016) 196, arXiv: 1512.01178 [hep-ph].

[41] R. Frederix and S. Frixione, *Merging meets matching in MC@NLO*, JHEP **12** (2012) 061, arXiv: 1209.6215 [hep-ph].

[42] R. Frederix, S. Frixione, E. Vryonidou and M. Wiesemann, *Heavy-quark mass effects in Higgs plus jets production*, JHEP **08** (2016) 006, arXiv: 1604.03017 [hep-ph].

[43] H. Mantler and M. Wiesemann, *Hadronic Higgs production through NLO + PS in the SM, the 2HDM and the MSSM*, Eur. Phys. J. C **75** (2015) 257, arXiv: 1504.06625 [hep-ph].

[44] H. Mantler and M. Wiesemann, *Top- and bottom-mass effects in hadronic Higgs production at small transverse momenta through LO+NLL*, Eur. Phys. J. C **73** (2013) 2467, arXiv: 1210.8263 [hep-ph].

[45] M. Cacciari, G. P. Salam and G. Soyez, *The anti-k_t jet clustering algorithm*, JHEP **04** (2008) 063, arXiv: 0802.1189 [hep-ph].

[46] ATLAS Collaboration, *Combined measurements of Higgs boson production and decay using up to 80 fb^{-1} of proton–proton collision data at $\sqrt{s}$ = 13 TeV collected with the ATLAS experiment*, Phys. Rev. D **101** (2020) 012002, arXiv: 1909.02845 [hep-ex].

[47] G. Cowan, K. Cranmer, E. Gross and O. Vitells, *Asymptotic formulae for likelihood-based tests of new physics*, Eur. Phys. J. C **71** (2011) 1554, arXiv: 1007.1727 [physics.data-an], Erratum: Eur. Phys. J. C **73** (2013) 2501.

[48] ATLAS Collaboration, *Fiducial and differential cross sections of Higgs boson production measured in the four-lepton decay channel in pp collisions at $\sqrt{s}$ = 8 TeV with the ATLAS detector*, Phys. Lett. B **738** (2014) 234, arXiv: 1408.3226 [hep-ex].

[49] ATLAS Collaboration, *Measurements of fiducial and differential cross sections for Higgs boson production in the diphoton decay channel at $\sqrt{s}$ = 8 TeV with ATLAS*, JHEP **09** (2014) 112, arXiv: 1407.4222 [hep-ex].

[50] ATLAS Collaboration, *Measurements of Higgs boson production and couplings in the four-lepton channel in pp collisions at center-of-mass energies of 7 and 8 TeV with the ATLAS detector*, Phys. Rev. D **91** (2015) 012006, arXiv: 1408.5191 [hep-ex].

[51] ATLAS Collaboration, *Measurement of Higgs boson production in the diphoton decay channel in pp collisions at center-of-mass energies of 7 and 8 TeV with the ATLAS detector*, Phys. Rev. D **90** (2014) 112015, arXiv: 1408.7084 [hep-ex].

[52] ATLAS Collaboration, *Measurements of the Total and Differential Higgs Boson Production Cross Sections Combining the $H \to \gamma\gamma$ and $H \to ZZ^* \to 4\ell$ Decay Channels at $\sqrt{s}$ = 8 TeV with the ATLAS Detector*, Phys. Rev. Lett. **115** (2015) 091801, arXiv: 1504.05833 [hep-ex].

[53] ATLAS Collaboration, *Measurements of Higgs boson properties in the diphoton decay channel with 36 fb^{-1} of pp collision data at $\sqrt{s}$ = 13 TeV with the ATLAS detector*, Phys. Rev. D **98** (2018) 052005, arXiv: 1802.04146 [hep-ex].

[54] CMS Collaboration, *Observation of Higgs Boson Decay to Bottom Quarks*, Phys. Rev. Lett. **121** (2018) 121801, arXiv: 1808.08242 [hep-ex].

[55] CMS Collaboration, *A search for the standard model Higgs boson decaying to charm quarks*, JHEP **03** (2020) 131, arXiv: 1912.01662 [hep-ex].

[56] ATLAS Collaboration,
A detailed map of Higgs boson interactions by the ATLAS experiment ten years after the discovery, CERN-EP-2022-057 (2022), arXiv: 2207.00092 [hep-ex].

[57] CMS Collaboration,
A portrait of the Higgs boson by the CMS experiment ten years after the discovery, CERN-EP-2022-039 (2022), arXiv: 2207.00043 [hep-ex].

[58] CMS Collaboration, *Search for Higgs boson decay to a charm quark-antiquark pair in proton-proton collisions at* $\sqrt{s} = 13$ *TeV*, CERN-EP-2022-081 (2022), arXiv: 2205.05550 [hep-ex].

[59] F. Bishara, U. Haisch, P. F. Monni and E. Re,
Constraining Light-Quark Yukawa Couplings from Higgs Distributions, Phys. Rev. Lett. **118** (2017) 121801, arXiv: 1606.09253 [hep-ph].

[60] M. A. Ebert, J. K. L. Michel, F. J. Tackmann et al.,
SCETlib: A C++ Package for Numerical Calculations in QCD and Soft-Collinear Effective Theory, DESY-17-099 (2018), webpage: http://scetlib.desy.de.

[61] G. Billis, B. Dehnadi, M. A. Ebert, J. K. L. Michel and F. J. Tackmann, *Higgs* p_T *Spectrum and Total Cross Section with Fiducial Cuts at Third Resummed and Fixed Order in QCD*, Phys. Rev. Lett. **127** (7 2021) 072001, arXiv: 2102.08039 [hep-ph].

[62] M. Bonvini, A. S. Papanastasiou and F. J. Tackmann,
Matched predictions for the $b\bar{b}H$ *cross section at the* 13 *TeV LHC*, JHEP **10** (2016) 053, arXiv: 1605.01733 [hep-ph].

[63] R. V. Harlander,
Higgs production in heavy-quark annihilation through next-to-next-to-leading order QCD, Eur. Phys. J. C **76** (2016) 252, arXiv: 1512.04901 [hep-ph].